Potassium–Sulfur Batteries

K_3SbS_4 as a Potassium Superionic Conductor with Low Activation Energy for K–S Batteries

Jieren Shao, Jingfeng Zheng, Lei Qin, Songwei Zhang, Yang Ren, and Yiying Wu*

Abstract: Solid-state K-ion conducting electrolytes are key elements to address the current problems in K secondary batteries. Here, we report a sulfide-based K-ion conductor K_3SbS_4 with a low-activation energy of 0.27 eV. W-doped $K_{3-x}Sb_{1-x}W_xS_4$ ($x = 0.04$, 0.06, 0.08, 0.10 and 0.12) compounds were also explored for increasing vacancy concentrations and improving ionic conductivity. Among them, $K_{2.92}Sb_{0.92}W_{0.08}S_4$ exhibits the highest conductivity of 1.4×10^{-4} S cm^{-1} at 40 °C, which is among the best reported potassium-ion conductors at ambient temperature. In addition, $K_{2.92}Sb_{0.92}W_{0.08}S_4$ is electrochemically stable with long-chained potassium polysulfide of K_2S_x. A room-temperature solid potassium–sulfur (K–S) battery system has therefore been successfully demonstrated, which is the first K–S battery prototype using non-commercial inorganic-based electrolyte to block the polysulfide shuttle.

$\mathbf{R}$echargeable potassium (K) metal batteries have emerged as promising solutions for large-scale energy storage beyond lithium-ion batteries. Owing to the high earth abundance, low cost, small shear modulus (0.661 GPa) and low redox potential (-2.93 V vs. SHE) offered by K, K secondary batteries including K-ion, K–oxygen (O_2) and K–sulfur (S) batteries have been recognized as the promising candidates, possessing high energy density and high critical current density.[1–6] However, the use of organic liquid electrolytes not only endangers the safety of these batteries, but also

[*] J. Shao, J. Zheng, Dr. L. Qin, S. Zhang, Prof. Y. Wu
Department of Chemistry and Biochemistry
The Ohio State University
100 West 18th Avenue, Columbus
OH 43210 (USA)
E-mail: wu@chemistry.ohio-state.edu

Dr. Y. Ren
X-ray Science Division
Argonne National Laboratory
Lemont, IL 60439 (USA)
and
Department of Physics, City University of Hong Kong
Kowloon, Hong Kong (P. R. China)

limits their cyclability due to O_2 crossover in K–O_2 batteries and polysulfide shuttling in K–S batteries. Non-flammable solid state electrolytes (SSEs) have shown the potential of effectively alleviating the abovementioned problems.[7,8] However, the research on K-ion conducting SSE is still at an early stage. As summarized by Johrendt et al., only a few oxide-based K-ion conductors are known with rare examples exceeding 10^{-4} S cm^{-1} at room temperature.[9] One such example is the commercial K-β″-alumina which shows ionic conductivity of 8×10^{-4} S cm^{-1} at room temperature.[10] To reduce the grain boundary resistance of K-β″-alumina, the sintering temperature is above 1000 °C, increasing the fabrication cost and thus limiting their practical applications.[11] More recently, Johrendt et al. reported the T5 KSi_2P_3 with ambient conductivity up to 2.6×10^{-4} S cm^{-1}, and our group reported the Ba-doped K_3OI antiperovskite, which possess excellent stability against reactive K metal.[9,12]

A useful strategy in searching for new K-ion conductors is to examine reported sodium superionic conductors. An interesting example is Na_3SbS_4 reported first in 2016 by three groups.[13–15] Zhang et al. reported the solid-state synthesis of tetragonal Na_3SbS_4 with ionic conductivity up to 3 mS cm^{-1}.[15] Wang et al. also reported an ionic conductivity of 1 mS cm^{-1} at 25 °C and pointed out its ambient stability in air.[13] Hong and Jung et al. further demonstrated the solution processibility of tetragonal Na_3SbS_4 that allows direct coating on electrode materials.[14] These pioneering efforts have inspired more experimental and theoretical research, especially in the effects of anion-, cation- or co-doping.[16–24] For example, Hayashi and co-workers then reported $Na_{2.88}Sb_{0.88}W_{0.12}S_4$ with room temperature conductivity of 3.2×10^{-2} S cm^{-1} via incorporating W^{6+} on the tetrahedral site.[22] The transition from the low-temperature tetragonal phase to the high-temperature cubic phase has also been investigated with the observation of an abnormally small activation energy of 0.036 eV for the cubic phase.[25]

Inspired by the superionic sulfide-based solid electrolytes with body-centered cubic (bcc) anion framework, we report a sulfide K-ion conductor β-K_3SbS_4 whose structure is close to bcc with minor distortions at room temperature. We further improve the ionic conductivity by increasing K^+ vacancy concentrations through W doping and achieve the room temperature solid K–S battery system using this new potassium superionic conductor.

The single crystal of β-K_3SbS_4 was first obtained in 1997 by mixing K_2S, Sb, Nb and S in a sealed quartz tube and heating at 350 °C for 6 days.[26] The final products are the mixtures of $K_6Nb_4S_{25}$ and K_3SbS_4, which requires further separation. Based on the reported structure, we have

applied geometrical-topological analysis to construct the K^+ cation migration map of β-K_3SbS_4 through the ToposPro software.[27] The topological analyses on the polyanions (SbS_4^{3-}) framework provide a map of void sites that are large enough to accommodate K^+ cations (labeled with numbers in Figure 1) and the diffusion channels with large cross-sectional bottlenecks (grey lines in Figure 1), indicat-
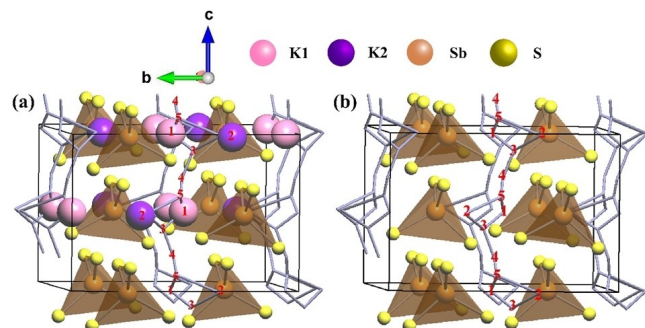

Figure 1. Geometrical-topological analysis of β-K_3SbS_4 via Topospro software. a) K^+ migration maps as Voronoi graphs (hereafter shown by gray lines) of voids ZA after considering the size of local space in the crystal structure framework, bond valence and cation distance. b) K^+ diffusion pathway after omitting all K ions.
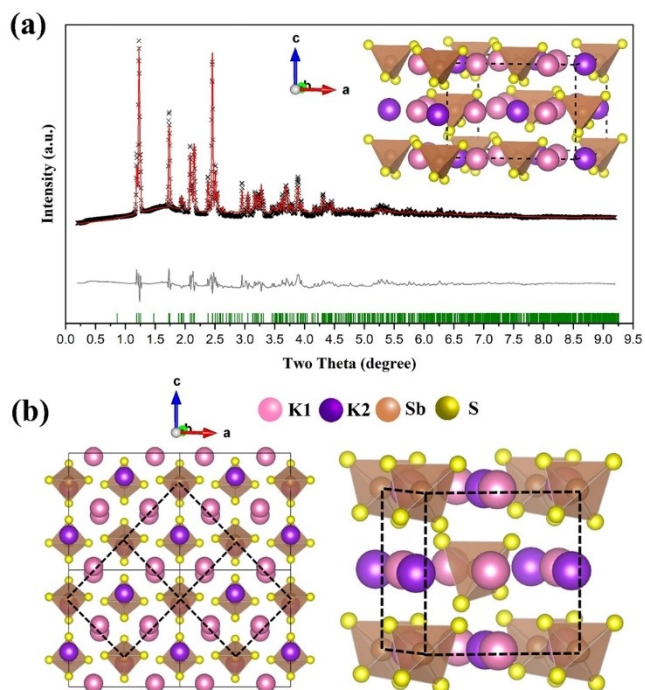

Figure 2. a) Rietveld refinement profiles of SXRD data for orthorhombic β-K_3SbS_4 ($a = 10.7306(16)$Å, $b = 11.2788(16)$Å, $c = 7.7091(11)$Å, $Z = 4$, space group $Cmc2_1$). Black dots and red lines denote the observed and calculated XRD patterns, respectively. The green sticks mark the position of the reflections for K_3SbS_4. The difference between the observed and calculated patterns is indicated by the grey line. The inset is the crystal structure of β-K_3SbS_4 with the unit cell outlined. b) Unit cells in the orthorhombic β-phase (left). The dotted lines cut out the distorted bcc polyanion framework of β-K_3SbS_4, which is shown on the right.

ing a two-dimensional K^+ diffusion network in β-K_3SbS_4. Detailed information of the analyses can be found in the Supporting Information (see Table S1 for the coordinates of all sites).

Inspired by the promising migration map, we then synthesized β-K_3SbS_4 via a one-step solid-state reaction at 550°C: $3K_2S + Sb_2S_3 + 2S = 2K_3SbS_4$. The experimental details on the solid-state syntheses can be found in the Supporting Information. Figure S1 shows the Raman spectra of pure K_3SbS_4. The characteristic asymmetric (n_a) and symmetric (n_s) stretching vibration peaks of the SbS_4^{3-} units in K_3SbS_4 are observed at around 360, 380, and 410 cm^{-1}, respectively, which is in good agreement with previous reports.[22] The Raman bands of the other starting materials (Sb_2S_3, K_2S and S) are not observed in the final product.

Figure 2a shows the synchrotron X-ray diffraction (SXRD, wavelength λ = 0.1173 Å) pattern of room-temperature β-K_3SbS_4 together with the corresponding whole pattern fitting refinement with reference to an orthorhombic structure of K_3SbS_4 ($a = 10.7306(16)$Å, $b = 11.2788(16)$Å, $c = 7.7091(11)$Å, $Z = 4$, space group $Cmc2_1$). Calculated R factor and structural parameters are summarized in Table S2 (Supporting Information). The crystal structure of orthorhombic β-K_3SbS_4 is shown in the inset of Figure 2a. The crystallographic unit cell consists of four distorted SbS_4 tetrahedron groups, with three types of S atoms whose atomic coordinates can be found in Table S1. Deviations from the ideal tetrahedral geometry are expressed by the S–Sb–S bond angles of 108.95° (S2–Sb–S2),109.52° (S2–Sb–S1), 109.53° (S2–Sb–S3) and 109.77°(S1–Sb–S3). Moreover, the Sb–S distances are 2.340 Å (Sb–S2), 2.347 Å (Sb–S1) and 2.353 Å (Sb–S3), respectively. As a result, the overall polar axis is along the c axis. Orthorhombic K_3SbS_4 possess two independent K positions: K1 at 8b and K2 at 4a sites. It is worth noting that the SbS_4 polyanions form a distorted bcc anion framework, which may benefit K^+ diffusion (Figure 2b).[28] Differential scanning calorimetry (DSC) curves of K_3SbS_4 are shown in Figure 3a. A reversible phase transition appears at 370°C during heating and 360°C during cooling, respectively. By using high-temperature SXRD, we have confirmed that β-K_3SbS_4 transform to α-K_3SbS_4 at high temperature. The corresponding whole pattern fitting refinement shows that α-K_3SbS_4 possesses the space group $\bar{P}43m$ with the lattice parameter $a = 7.847$ Å, where the unit cell consists of a body-centered sub-lattice with SbS_4^{3-} (Figure S2, Table S3). In contrast to β-K_3SbS_4 where K atoms situate at two different positions, α-K_3SbS_4 possesses one K position simply located at the 6b site. Moreover, the SbS_4 groups here possess an ideal tetrahedral geometry with the S–Sb–S bond angles of 109.5° and Sb–S bonds length of 2.365 Å. To our best knowledge, this is the first time to measure the phase transformation temperature of K_3SbS_4.

The conductivity of the hot-pressed K_3SbS_4 pellet was measured by the alternating current (AC) impedance method. The Nyquist plot of K_3SbS_4 measured at room temperature was fitted with the equivalent circuit shown in the insert of Figure 3b. The fitted parameters are listed in Table S4. Since it is difficult to separate the bulk and grain
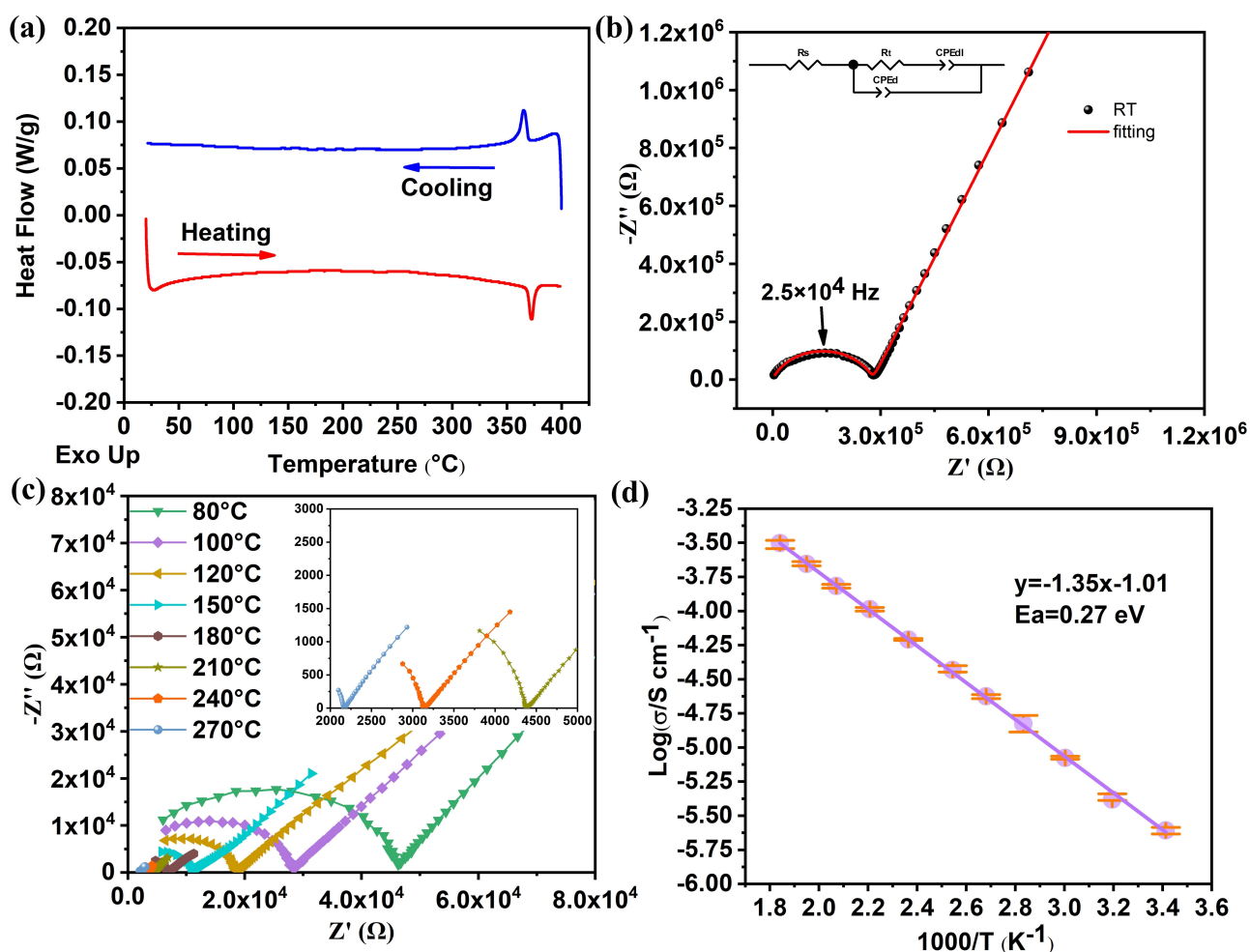
Figure 3. Characterizations of undoped K_3SbS_4 samples. a) Differential Scanning Calorimetry (DSC) data collected at a heating rate of $5\,°C\,min^{-1}$ in a flow of dry nitrogen gas. b) Impedance spectroscopy Nyquist plot of K_3SbS_4 sample at room temperature, showing the experimental data (black) and the fitting result from the equivalent circuit model (red). Rs is the inner resistance of the set-up (cell+wire); Rt is the total resistance of the electrolyte, including both the bulk resistance and grain boundary resistance; CPEdl is the constant phase element of the blocking electrode-electrolyte interface; CPEd is the constant phase element of the bulk pellet sandwiched between the two blocking electrodes. c) Nyquist plots of K_3SbS_4 sample at different temperatures. d) The Arrhenius plot of the average K ion conductivity of the K_3SbS_4 electrolyte, revealing an activation energy of 0.27 eV. Vertical error bars represent the standard error of mean of three batches of K_3SbS_4.

boundary resistance, the total conductivity is calculated from the total resistance (R_t). Figure 3c displays the Nyquist plots of the ionic conductivity of the K_3SbS_4 electrolyte in the temperature range of 20–270 °C, using the high-temperature adaptive Swagelok electrochemical cell. The Arrhenius plot of the average ionic conductivity of K_3SbS_4 from three batches is shown in Figure 3d. The temperature dependence of ionic conductivity follows the Arrhenius equation ($\sigma = \sigma_0 * e^{-E_a/kT}$), where σ_0 denotes the temperature-independent ionic conductivity, k represents the Boltzmann constant, and E_a denotes the activation energy. The calculated average ionic conductivity is $2.5 \times 10^{-6}\,S\,cm^{-1}$ at room temperature and $1.0 \times 10^{-4}\,S\,cm^{-1}$ at 180 °C. The Arrhenius plot for hot-pressed K_3SbS_4 is linearly fitted with an activation energy of 0.27 eV, indicating the low K^+ migration energy barrier along the conduction path. Such E_a value is among the lowest ones and even comparable with that of K-β''-alumina.[10]

Previous studies have demonstrated the improvement of the ionic conductivity of Na_3SbS_4 by partially incorporating W^{6+} on the tetrahedral sites, leading to the increase of vacancy concentrations through charge compensation.[16,17,19,22] Following the similar logics, the effect of doping on the ionic conductivity of K_3SbS_4 compound was then investigated, given that an undoped K_3SbS_4 possess fully occupied K^+ positions and thus exhibits a low mobile ion concentration. To synthesize W-doped $K_{3-x}Sb_{1-x}W_xS_4$ ($x = 0.04$, 0.06, 0.08, 0.10 and 0.12), we mixed WS_2, K_2S, Sb_2S_3, and S and repeated the previous preparation process. Due to the high melting point of WS_2, the pellet for synthesis was heated at 800 °C for 24 h. The powder X-ray diffraction data of $K_{3-x}Sb_{1-x}W_xS_4$ ($x = 0.04$, 0.06, 0.08, 0.10 and 0.12) are shown in Figure S3. No apparent peak shift in the PXRD patterns is observed with increasing x. This is probably because of the nearly same ionic radii of Sb^{5+} and W^{6+}. Raman was further used to monitor the

generation of WS_4^{2-} tetrahedra within the structure. In the Raman spectra of $K_{3-x}Sb_{1-x}W_xS_4$ ($x=0.04$, 0.06, 0.08, 0.10 and 0.12), three Raman peaks can be noticed in the range of 340 to 410 cm^{-1}, corresponding to the different modes of the SbS_4^{3-} tetrahedra in $K_{3-x}Sb_{1-x}W_xS_4$ (Figure S1 and Figure S3). With increasing the W content, additional Raman-active modes can be found in the range of 450 to 500 cm^{-1}, corresponding to the symmetric and asymmetric vibration of WS_4^{2-} (shown in green).[22]

To gain insights into how the increasing K$^+$ vacancy concentration affects the ionic transport properties. AC impedance spectroscopy was performed on $K_{3-x}Sb_{1-x}W_xS_4$. Figure 4a shows the room temperature ionic conductivity for hot-pressed $K_{3-x}Sb_{1-x}W_xS_4$. Among them, $K_{2.92}Sb_{0.92}W_{0.08}S_4$ exhibits the highest room temperature (20°C) conductivity of 7.7×10^{-5} S cm^{-1} in a sintered body (Figure 4a, Figure S4 and Figure S5). However, when further increasing the W dopant concentrations, the products contain some impur-

ities, which probably cause the decrease of the ionic conductivity (Figure S6). Therefore, investigations on K$^+$ vacancies effect are mainly focused on the $K_{3-x}Sb_{1-x}W_xS_4$ ($x=0.04$, 0.06, and 0.08). The Arrhenius plots of the K-ion conductivity of the $K_{3-x}Sb_{1-x}W_xS_4$ ($x=0$, 0.04, 0.06, and 0.08) electrolytes are shown in Figure 4b. With increasing W contents, the activation barriers for ion migration did not change in this series of compounds, indicating that the K migration pathway was unaffected by moderate W doping.

The crystalline structure and electrochemical properties of $K_{2.92}Sb_{0.92}W_{0.08}S_4$ are also investigated and discussed. Compared to that of K_3SbS_4, the phase transition temperature of $K_{2.92}Sb_{0.92}W_{0.08}S_4$ decreases, while the space groups of the room-temperature and high-temperature compounds did not change (Figure S7, Figure S8 and Figure S9). In addition, the occupancy of K1 sites decreases around 8%, indicating the success of K vacancy injection (Table S5, Table S6). The electrochemical window of $K_{2.92}Sb_{0.92}W_{0.08}S_4$
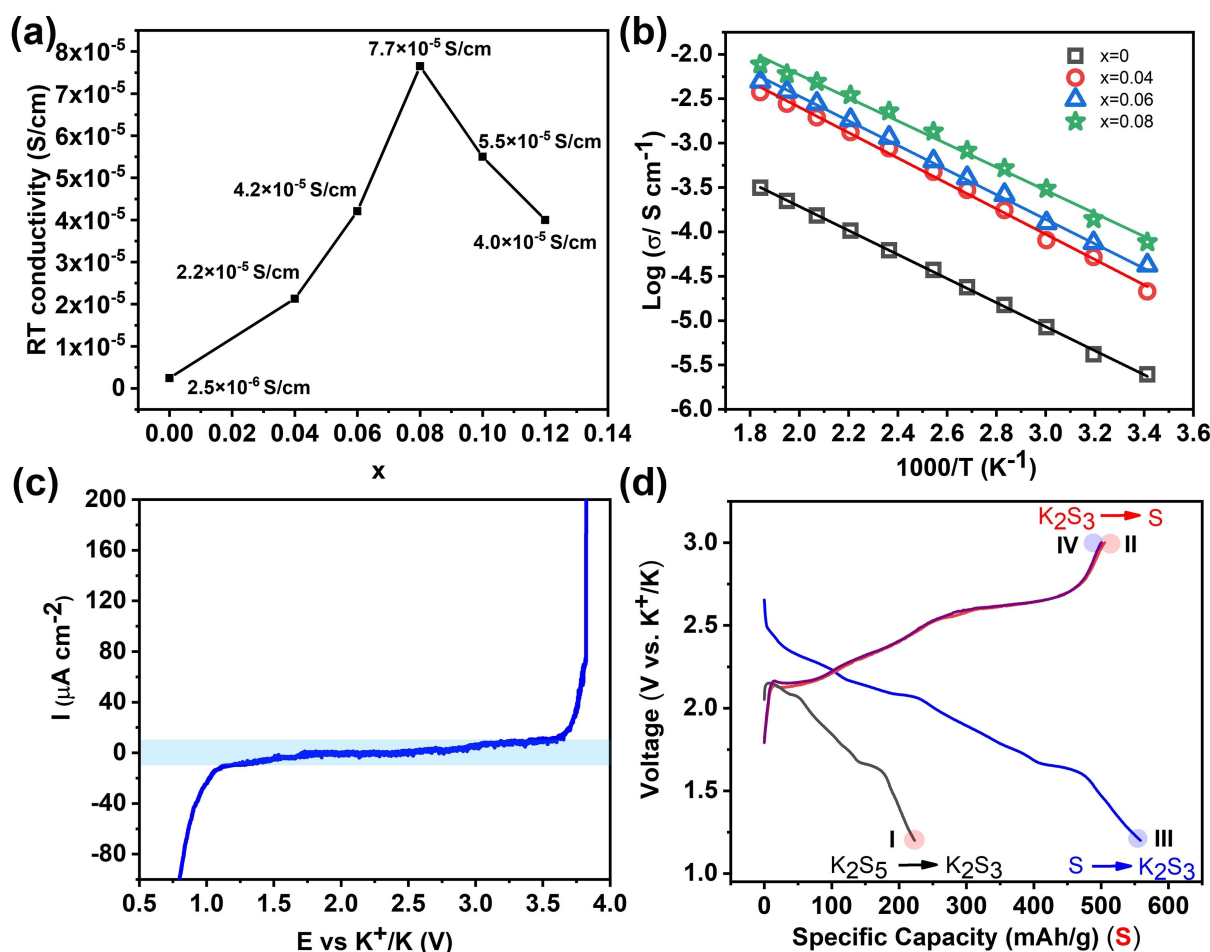

Figure 4. a) Conductivity at 20°C for conduction of the $K_{3-x}Sb_{1-x}W_xS_4$ ($x=0.04$, 0.06, 0.08, 0.10 and 0.12) pellets prepared by hot-pressing at 400 MPa and 150°C for 1 hour, followed by heat treatment at 400°C for 1 hour. b) The Arrhenius plots of the K ion conductivity of the $K_{3-x}Sb_{1-x}W_xS_4$ ($x=0$, 0.04, 0.06, and 0.08) electrolytes, revealing an unchanged activation energy of 0.27 eV. c) LSV curve of the $K_{2.92}Sb_{0.92}W_{0.08}S_4$ at 20°C at the scan rate of 0.1 mV s^{-1}. In the light blue region, the current density is below 10 μA cm^{-2}. There is no significant anodic current density shown up to 3.5 V, indicating that $K_{2.92}Sb_{0.92}W_{0.08}S_4$ is electrochemically stable up to 3.5 V vs. K$^+$/K. d) Charge–discharge curves of the K–S cell at the current of 15 mA between 1.2 and 3.0 V versus K/K$^+$ for the first two cycles. I and III are the discharge products of the 1st and 2nd cycles, respectively, while II and IV are the corresponding charging products. In process III, the disproportion reaction product K_2S_5 can be further reduced to K_2S_3 during the discharge process and thus the capacity in state III is higher than that in state II.

was measured by linear sweep voltammetry (LSV) at a scan rate of $0.1\,mV\,s^{-1}$ (Figure 4c). The measurement was performed on the cell configuration of K metal/1 M KFSI-DME/$K_{2.92}Sb_{0.92}W_{0.08}S_4$-carbon paper. Details of the fabrication of the $K_{2.92}Sb_{0.92}W_{0.08}S_4$ cathode and LSV measurements can be found in the Supporting Information. The LSV curve suggests that $K_{2.92}Sb_{0.92}W_{0.08}S_4$ is thermodynamically stable up to 3.5 V vs. K^+/K. To exclude the interference from the decomposition of liquid electrolyte, the electrochemical window of bulk low-concentration electrolyte (LCE) was also estimated (Figure S10). Note that there is no obvious anodic current induced up to 4 V and the cathodic current occurs below 1.2 V for LCE. Therefore $K_{2.92}Sb_{0.92}W_{0.08}S_4$ is electrochemically stable within 1.5 V–3.5 V vs. K^+/K.

To confirm that K^+ is the mobile charge carrier in $K_{2.92}Sb_{0.92}W_{0.08}S_4$ and to test the electrolyte performance, we fabricated a solution-phase long-chain potassium polysulfide (K_2S_x) symmetric cell in which the $K_{2.92}Sb_{0.92}W_{0.08}S_4$ solid state electrolyte pellet was sandwiched by the K_2S_x soaked carbon paper. First, long-chained K_2S_x ($4 \leq x \leq 6$) was prepared by mixing commercial short-chained polysulfide (dominant product of K_2S_3) and S in a molar ratio of 1:2 with DEGDME as the solvating solvent (Figure S11). The solution-phase K_2S_x exhibits a typical dark brown solution and contains the mixture of S_4^{2-}, S_5^{2-} and S_3^- radical (S_6^{2-}), as confirmed by the UV/Vis spectroscopy (Figure S12). Then the cycling performance of the K_2S_x symmetric cell was evaluated at 20 °C. The overpotential of the symmetric cell was 7 mV at a current density of $5\,\mu A\,cm^{-2}$ (Figure S13). The ionic conductivity calculated from the electrolyte resistance is $7.3 \times 10^{-5}\,S\,cm^{-1}$, which matches well with the previous measured value of $7.7 \times 10^{-5}\,S\,cm^{-1}$ from ionic conductivity measurement. After 100 cycles, the current density was gradually increased to $10\,\mu A\,cm^{-2}$, $25\,\mu A\,cm^{-2}$, $50\,\mu A\,cm^{-2}$, and $0.1\,mA\,cm^{-2}$. The cell operates for 100 cycles under each current density and delivers good cycling performance (Figure S13a).

Inspired by the decent ionic conductivity and excellent electrochemical stability of $K_{2.92}Sb_{0.92}W_{0.08}S_4$ against potassium polysulfide, a proof-of-concept solid K–S battery was demonstrated at room temperature. Our proposed sulfide-based compound was used as the SSE. Figure S14 shows the schematic illustration of the two-compartment K–S cell configuration (See the detailed information in the Supporting Information). A solution-phase K_2S_x ($4 \leq x \leq 6$) catholyte was selected as the starting material, which was soaked into a piece of carbon paper. The cell was initially discharged to 1.2 V at a 0.5 C-rate and then charged back to the cut-off voltage of 3 V (Figure 4d). Based on the previous literatures, the higher reduction plateau appearing at ≈ 2.0 V at the 2nd discharge process can be assigned to the formation of high-order K_2S_x ($5 \leq x \leq 6$) from sulfur reduction, while the lower reduction plateau at ≈ 1.6 V can be ascribed to the transition from K_2S_x ($5 \leq x \leq 6$) to the low-order potassium polysulfide of K_2S_3.[29,30]

The initial discharge and charge products were further analyzed by ex situ Raman spectroscopy (Figure S15). After the first discharge, the Raman spectrum showed a peak at $465\,cm^{-1}$, originating from the formation of K_2S_3. After the

subsequent first charge, the corresponding product is assigned to sulfur. Note that the 1st discharge capacity of $220\,mAh\,g^{-1}$ is lower than the 1st charge capacity of $556\,mAh\,g^{-1}$. The corresponding capacities are related to the conversion processes of $K_2S_5 \rightarrow K_2S_3$ (discharge) and $K_2S_3 \rightarrow S$ (charge), respectively, which is close to the theoretical capacities of $K_2S_5 \rightarrow K_2S_3$ ($223.4\,mAh\,g^{-1}$) and $K_2S_3 \rightarrow S$ ($558.5\,mAh\,g^{-1}$). The galvanostatic charge curves for the first two cycles overlap. Moreover, the discharge and charge products of the second cycle were also analyzed and matches well with those after the first cycle, indicating that this process has a good reversibility initially. Nevertheless, the proposed solid K–S battery only shows a capacity retention of 55% after 40 cycles with the average coulombic efficiency of 92% at 0.5 C-rate (Figure S16).

Post-mortem analyses were conducted on the cycled S cathode to reveal the underlying capacity decay mechanism. The 1st full discharged cathode was aged for 1 week and the corresponding products were analyzed to evaluate the shelf-life of discharge products. It is obvious to observe the additional K_2S_5 together with parent K_2S_3 based on the X-ray photoelectron spectroscopy (XPS) and Raman analyses (Figure S17). This indicates that the disproportion reaction of K_2S_3 ($2K_2S_3 \rightarrow K_2S + K_2S_5$) may occur spontaneously during the aging process. In addition, the specific discharge capacity is larger than that of the previous charge one (Figure S16). Based on our current understanding, the extra discharge capacity may be ascribed to the electrochemical reduction of long-chained potassium polysulfide, which was formed through the disproportionation reaction (Scheme S1). The abovementioned side reactions related to the K_2S formation may also occur in the battery cycling process. Notably, the K_2S is thought to be electrochemically inactive in K–S batteries system based on the previous studies, thus responsible for the gradual capacity decay.[31–33] Nevertheless, it is still encouraging to observe that the SSE can block the polysulfide shuttle, which is one of the major problems of current K–S batteries system, as the surface of protected potassium electrode does not show any side products assigned to K_2S or potassium polysulfide. The XPS spectrum indicates that there are sulfate/thiosulfate complex species (RSO_x), most likely due to the decomposition of KTFSI supporting salt in the catholyte (Figure S18a). In comparison, we also constructed the conventional K–S cell setup but without adding the SSE. The unprotected K anode turned dark brown after the initial cycle and the K_2S species is identified based on the XPS S 2p spectrum (Figure S18b). Such a cell delivers a reduced discharge capacity due to self-discharging and shows the typical endless charging behavior, which was induced by the side reactions between the K anode and high-order polysulfide shuttling from the cathode (Figure S19). According to the discussions above, it can clearly be seen that the use of a solvent-impermeable SSE can block the shuttle of potassium polysulfide, though further optimization on catholyte recipe or cathode microstructure is still required to facilitate the decomposition of K_2S.

In summary, this work reports K_3SbS_4 as a promising sulfide-based K-ion conductor with a two-dimensional K

migration pathway at room temperature, a room-temperature ionic conductivity of 2.5×10^{-6} S cm^{-1} and an activation energy of 0.27 eV. Through aliovalent substitution, $K_{3-x}Sb_{1-x}W_xS_4$ ($x = 0.04$, 0.06, 0.08, 0.10 and 0.12) were synthesized with enhanced vacancy concentrations and improved ionic conductivity. Among them, the optimized $K_{2.92}Sb_{0.92}W_{0.08}S_4$ exhibits the ionic conductivity of 7.7×10^{-5} S cm^{-1} at room temperature and 1.4×10^{-4} S cm^{-1} at 40 °C, which is remarkably high for a K-ion conductor at ambient temperature. A two-compartment solid K–S battery prototype has therefore been demonstrated and further operated at room temperature, which is the first K–S battery prototype using non-commercial inorganic-based electrolyte to address the polysulfide shuttle issue.

Conflict of Interest

The authors declare no conflict of interest.

Data Availability Statement

The data that support the findings of this study are available from the corresponding author upon reasonable request.

[1] R. J. Y. Park, C. M. Eschler, C. D. Fincher, A. F. Badel, P. Guan, M. Pharr, B. W. Sheldon, W. C. Carter, V. Viswanathan, Y. M. Chiang, *Nat. Energy* **2021**, *6*, 314.

[2] L. Qin, L. Schkeryantz, J. Zheng, N. Xiao, Y. Wu, *J. Am. Chem. Soc.* **2020**, *142*, 11629.

[3] N. Xiao, X. Ren, W. D. McCulloch, G. Gourdin, Y. Wu, *Acc. Chem. Res.* **2018**, *51*, 2335.

[4] J. Y. Hwang, S. T. Myung, Y. K. Sun, *Adv. Funct. Mater.* **2018**, *28*, 1802938.

[5] D. J. Kim, D.-J. Yoo, M. T. Otley, A. Prokofjevs, C. Pezzato, M. Owczarek, S. J. Lee, J. W. Choi, J. F. Stoddart, *Nat. Energy* **2019**, *4*, 51.

[6] T. Hosaka, K. Kubota, A. S. Hameed, S. Komaba, *Chem. Rev.* **2020**, *120*, 6358.

[7] X. Chen, W. He, L. X. Ding, S. Wang, H. Wang, *Energy Environ. Sci.* **2019**, *12*, 938.

[8] Z. Jiang, S. Wang, X. Chen, W. Yang, X. Yao, X. Hu, Q. Han, H. Wang, *Adv. Mater.* **2020**, *32*, 1906221.

[9] A. Haffner, A. K. Hatz, O. E. O. Zeman, C. Hoch, B. V. Lotsch, D. Johrendt, *Angew. Chem. Int. Ed.* **2021**, *60*, 13641; *Angew. Chem.* **2021**, *133*, 13754.

[10] A. C. Baclig, G. McConohy, A. Poletayev, A. Michelson, N. Kong, J. H. Lee, W. C. Chueh, J. Rugolo, *Joule* **2018**, *2*, 1287.

[11] Z. Zhang, Y. Shao, B. Lotsch, Y. S. Hu, H. Li, J. Janek, L. F. Nazar, C. W. Nan, J. Maier, M. Armand, L. Chen, *Energy Environ. Sci.* **2018**, *11*, 1945.

[12] J. Zheng, H. Fang, L. Fan, Y. Ren, P. Jena, Y. Wu, *J. Phys. Chem. Lett.* **2021**, *12*, 7120.

[13] H. Wang, Y. Chen, Z. D. Hood, G. Sahu, A. S. Pandian, J. K. Keum, K. An, C. Liang, *Angew. Chem. Int. Ed.* **2016**, *55*, 8551; *Angew. Chem.* **2016**, *128*, 8693.

[14] A. Banerjee, K. H. Park, J. W. Heo, Y. J. Nam, C. K. Moon, S. M. Oh, S. T. Hong, Y. S. Jung, *Angew. Chem. Int. Ed.* **2016**, *55*, 9634; *Angew. Chem.* **2016**, *128*, 9786.

[15] L. Zhang, D. Zhang, K. Yang, X. Yan, L. Wang, J. Mi, B. Xu, Y. Li, *Adv. Sci.* **2016**, *3*, 1600089.

[16] F. Tsuji, N. Masuzawa, A. Sakuda, M. Tatsumisago, A. Hayashi, *ACS Appl. Energy Mater.* **2020**, *3*, 11706.

[17] H. Gamo, N. H. H. Phuc, H. Muto, A. Matsuda, *ACS Appl. Energy Mater.* **2021**, *4*, 6125.

[18] J. W. Heo, A. Banerjee, H. Kern, Y. Park, J. Seok, S.-T. Hong, J. W. Heo, S.-T. Hong, A. Banerjee, K. H. Park, Y. S. Jung, *Adv. Energy Mater.* **2018**, *8*, 1702716.

[19] X. Zhang, K. C. Phuah, S. Adams, *Chem. Mater.* **2021**, *33*, 9184.

[20] R. Jalem, B. Gao, H.-K. Tian, Y. Tateyama, *J. Mater. Chem. A* **2022**, *10*, 2235–2248.

[21] H. Wan, J. P. Mwizerwa, F. Han, W. Weng, J. Yang, C. Wang, X. Yao, *Nano Energy* **2019**, *66*, 104109.

[22] A. Hayashi, N. Masuzawa, S. Yubuchi, F. Tsuji, C. Hotehama, A. Sakuda, M. Tatsumisago, *Nat. Commun.* **2019**, *10*, 5266.

[23] S. Xiong, Z. Liu, H. Rong, H. Wang, M. McDaniel, H. Chen, *Sci. Rep.* **2018**, *8*, 9146.

[24] H. Gamo, H. H. P. Nguyen, R. Matsuda, H. Muto, A. Matsuda, *Solid State Ionics* **2020**, *344*, 115133.

[25] Q. Zhang, C. Zhang, Z. D. Hood, M. Chi, C. Liang, N. H. Jalarvo, M. Yu, H. Wang, *Chem. Mater.* **2020**, *32*, 2264.

[26] H. A. Graf, H. Schäfer, *ZAAC* **1976**, *425*, 67.

[27] V. A. Blatov, A. P. Shevchenko, D. M. Proserpio, *Cryst. Growth Des.* **2014**, *14*, 3576.

[28] Y. Wang, W. D. Richards, S. P. Ong, L. J. Miara, J. C. Kim, Y. Mo, G. Ceder, *Nat. Mater.* **2015**, *14*, 1026.

[29] S. Gu, N. Xiao, F. Wu, Y. Bai, C. Wu, Y. Wu, *ACS Energy Lett.* **2018**, *3*, 2858.

[30] J. Y. Hwang, H. M. Kim, C. S. Yoon, Y. K. Sun, *ACS Energy Lett.* **2018**, *3*, 540.

[31] J. Ding, H. Zhang, W. Fan, C. Zhong, W. Hu, D. Mitlin, *Adv. Mater.* **2020**, *32*, 1908007.

[32] X. Zhao, Y. Lu, Z. Qian, R. Wang, Z. Guo, *EcoMat* **2020**, *2*, e12038.

[33] C. Ye, J. Shan, D. Chao, P. Liang, Y. Jiao, J. Hao, Q. Gu, K. Davey, H. Wang, S.-Z. Qiao, *J. Am. Chem. Soc.* **2021**, *143*, 16902–16907.